OPEN ACCESS
Journal of Innovative Optical Health Sciences
Vol. 16, No. 5 (2023) 2350005 (10 pages)

DOI: 10.1142/S1793545823500050

World Scientific
www.worldscientific.com

# Transmissive multifocal laser speckle contrast imaging through thick tissue

Ruoyu Chen, Peng Miao* and Shanbao Tong
*School of Biomedical Engineering*
*Shanghai Jiao Tong University*
*800 Dongchuan Rd., Shanghai 200240, P. R. China*
**pengmiao@sjtu.edu.cn*

Received 24 October 2022
Accepted 8 January 2023
Published 17 March 2023

Laser speckle contrast imaging (LSCI) is a powerful tool for monitoring blood flow changes in tissue or vessels *in vivo*, but its applications are limited by shallow penetration depth under reflective imaging configuration. The traditional LSCI setup has been used in transmissive imaging for depth extension up to $2l_t$–$3l_t$ ($l_t$ is the transport mean free path), but the blood flow estimation is biased due to the depth uncertainty in large depth of field (DOF) images. In this study, we propose a transmissive multifocal LSCI for depth-resolved blood flow in thick tissue, further extending the transmissive LSCI for tissue thickness up to $12l_t$. The limited-DOF imaging system is applied to the multifocal acquisition, and the depth of the vessel is estimated using a robust visibility parameter $V_r$ in the coherent domain. The accuracy and linearity of depth estimation are tested by Monte Carlo simulations. Based on the proposed method, the model of contrast analysis resolving the depth information is established and verified in a phantom experiment. We demonstrated its effectiveness in acquiring depth-resolved vessel structures and flow dynamics in *in vivo* imaging of chick embryos.

*Keywords*: Transmissive imaging; multifocal imaging; depth; laser speckle contrast model.

## 1. Introduction

Laser speckle contrast imaging (LSCI) is a wide-field high-resolution optical imaging technique with simple implementation to measure blood flow changes *in vivo*.[1–3] Based on the speckle patterns derived from random interference of scattered coherent light, the local dynamics of the moving scatters (e.g., red blood cells) can be quantified by a speckle contrast $K$ to decorrelation time $\tau_c$ model with prior knowledge of scattering regime and velocity distribution.[4] The conventional LSCI works under a backscattering configuration, which is

*Corresponding author.

suitable for monitoring blood flow and perfusion in superficial tissues such as skin, retina and cerebral cortex. It is shown by Monte Carlo simulation (MCS) that most detected signals come from the top 700 $\mu$m brain-like tissue with a near infrared illumination.[5] The depth is suitable for imaging pial vessels with a cranial window in rat, however, deeper vessels in a 2D speckle contrast image can lead to ambiguity in interpreting blood flow velocity,[6] because depth itself contributes to correlation loss and thus the decrease in speckle contrast value. To acquire dynamic intravascular signals from deeper tissue, researchers developed a transmissive-detected LSCI (TR-LSCI) setup with one-way forward-scattering geometry. Li *et al.* systematically evaluated the performance of TR-LSCI and found that it achieved a much stronger signal-to-background ratio in thick tissue than conventional LSCI.[7] The vessel depth in transmissive LSCI, however, is still not yet well resolved. The depth information is also critical for correcting the calculated blood flow.

Multifocal imaging is a fast and easy-to-implement 3D imaging method to obtain depth information.[8] For imaging systems with limited depth of field (DOF), out-of-focus structures are blurred by the point spread function (PSF), resulting in widened boundaries and overestimated intensities of absorbing objects. This dependency is used in the "depth-from-defocus" (DFD) method to infer the depth of an object relative to the focal plane based on image properties such as sharpness and intensity. In LSCI, the dynamic fraction $\rho$ of the time-averaged intensity can be used as a DFD cue since it behaves similarly as the incoherent intensity.[9] On the other hand, when the imaging depth exceeds the system's DOF, either due to the imaging depth extension with a transmissive setup, or the decrease of DOF by a microscopic imaging system,[10] the defocus effect should be taken into account to minimize the error in estimation of speckle contrast. Several groups have proposed methods to improve focusing in LSCI, for example, Ringuette combined kurtosis and cross-variance to enable the localization of best focus in an autofocus system,[11] Zheng measured the system PSF and then implemented a deconvolution method to correct the out-of-focus blur and retrieve the vessel depth,[9] Du used a line-scanning confocal imaging setup and realized microscopic depth sectioning.[12] However, these methods have only been applied to reflective systems with imaging depth less than 500 $\mu$m. DFD methods so far haven't yet been validated for transmissive thick tissue imaging when both intensity and correlation attenuation from multiple scattering are to play an important role.

A simplified laser speckle contrast model estimates the blood flow index as $1/K^2$, which is widely adopted in conventional real-time LSCI applications for its numerical simplicity. However, this estimation relies on several assumptions that may not be satisfied in practical situations,[13] in particular, the absence of static scattering. Since visible but deep vessels usually have larger diameters, depth-dependent static scattering thus should be taken into account to avoid underestimating the intravascular flow velocities. A rigorous model between the speckle contrast and the decorrelation time was proposed in multi-exposure laser speckle imaging (MESI),[14] by introducing the dynamic scattering fraction $\rho$ into the intensity autocorrelation function $g_2(\tau)$. MESI uses multi-exposure speckle contrast images to fit all the parameters and thus obtain more robust flow measurement in the presence of static scattering. In transmissive multifocal LSCI, the dynamic scattering fraction of the target vessel can be retrieved in an easier way. We demonstrate $\rho$ decays exponentially with depth in the transmissive imaging setup with MCS.[15] With an assumption of multiple scattering regime and ordered motion of blood cells, the speckle contrast can then be modeled as a function of decorrelation time $\tau_c$ and depth.[16] Based on the depth information retrieved from multifocal images, unbiased blood flow index can be directly calculated from the in-focus speckle contrast image.

In this study, we propose a transmissive multifocal LSCI method to reconstruct 3D blood flow images in thick tissue. The multifocal laser speckle images are first analyzed along the vessel centerline to determine the vessel depth based on the DFD method. The depth map together with in-focus speckle contrast is then fitted with the transmissive speckle contrast model to get the blood flow in the form of the inverse decorrelation time $1/\tau_c$. Our method enables the extension of transmissive LSCI for tissue thickness up to $12l_t$ by correctly resolving the blood flow in the last $2l_t$. We tested the reliability and consistency of our method using electric field Monte Carlo and a phantom experiment, and demonstrated the effectiveness of transmissive 3D blood flow imaging in a chick embryo.

## 2. Materials and Methods

### 2.1. *Transmissive laser speckle imaging*

Traditional LSCI works in the reflective imaging geometry using a large DOF lens. For incoherent imaging in natural scenes, DOF ($L_F$) is a manufacturing parameter of the lens system and determines the depth of perfect imaging $L_D = L_F$. For coherent imaging of the random medium, e.g., LSCI, $L_D$ is further limited by the transport mean free path $l_t$ (i.e., $L_D \approx 1l_t$), within which the blood flow and vasculature can be well-estimated by analyzing the speckle patterns. The transport mean free path $l_t$ is dependent on the tissue's absorption coefficient ($\mu_a$) and reduced scattering coefficient ($\mu_s'$) in a relation of $l_t = 1/(\mu_a + \mu_s')$. Thus, traditional LSCI has $L_D \approx 750\,\mu\text{m} < L_F$ when working with 780–850 nm coherent light.[5]

Traditional LSCI utilizes a backscattering configuration; therefore, the round trip of backscattered light significantly limits $L_D$. Transmissive imaging geometry[9] is a straightforward way to extend $L_D \approx 2l_t$ by switching to one-way propagation. This improvement succeeds in the tissue thickness of $L \leq 2l_t - 3l_t$.[7] For thicker tissue ($L \approx 4l_t - 12l_t$), the transmitted laser light produces speckle patterns which can be modeled as the diffusion (static) part and dynamic part. In this regime, coherent light propagation can be approximated as a two-stage procedure (Fig. 1): (1) coherent light propagates from the incident surface to the deepest imaging plane ($L_P \leq 10l_t$); (2) the generated dynamically speckled light field illuminates the tissue volume within the imaging depth ($L_D = 2l_t$). Traditional LSCI failed in blood flow estimation due to the randomly distributed light field and depth uncertainty of vessels.[17] The use of a large DOF lens further introduces significant out-of-focus blur. In this study, we propose a multifocal strategy to estimate the vessel depth and achieve blood flow imaging up to the thickness $L_D \approx 2l_t$ from the exit plane of the thick tissue ($L \approx 4l_t - 12l_t$).

In stage-1, phase coherence among different propagating paths produces a speckle phenomenon when coherent light transmits through the random medium. In a homogeneous and purely scattering random medium, an $L_P \approx l_s$ propagation produces the fully developed speckle pattern. A thicker random medium ($L_P > l_s$) degenerates the speckle patterns due to the diffusion in the intensity domain. The speckles $I(t)$ on the $L_P$ plane are thus hybrid of diffusion and fully developed speckles, i.e., $I(t) = I_d(t) + I_s(t)$. After sufficient propagation, i.e., $L_P \gg l_t$, the coherent light eventually loses its phase coherence, and the speckles disappear.

LSCI utilizes the contrast ($K$) parameter of speckle pattern as a proxy of the blood flow velocity. Successful detection of blood flow requires $K > 2/\text{SNR}$ after $L = L_P + L_D$ propagation. The signal-to-noise ratio (SNR) of modern CCD/CMOS system is usually more than 30 dB, i.e., SNR = 1000, or $K > 0.002$, which determines the upper limit of $L$. Another factor affecting $L$ is the method for calculating the contrast $K$. Traditional LSCI utilizes either a spatial or temporal window, i.e., $K_s$ or $K_t$, to estimate the blood flow velocity. The $K_s$ parameter could be further biased by the structural inhomogeneity after more transmissive propagation ($L > 4l_t$). Therefore, the temporal contrast $K_t$ is more desirable for blood flow imaging. The upper bound of thickness $L$ is estimated based on MCS. Figure 1 shows that $K_t$ degenerates with the increase in $L$, assuming that a coherent and linearly polarized plane wave illuminates the left surface of the random medium. Ideally, the criterion $K_t > 0.002$ leads the $L$ up to $15l_t$. In practice, the nonideal coherent of light source[18] and aberrations in the lens system limits the $L$. Thus, $L < 12l_t$ should be the upper bound considered in this study.

In stage-2, the tissue volume (depth: $L_D$) is illuminated by the dynamic speckle $I(t)$ on the $L_P$ plane. Then, the transmitted speckle patterns $I_t(t)$ are captured by a focus imaging system. The dynamic speckle illuminations on the $L_P$ plane introduce additional difficulties in explaining of the contrast value calculated from $I_t(t)$. In order to estimate the blood flow more accurately, we need to include the depth information in the explanatory variables. Traditional LSCI, however, uses an imaging system with $L_F > L_D$, which aggregates the information in all depths. In this study, we use a limited DOF $L_F < L_D$ imaging system and perform multifocus detection (MFD) that can resolve the depth information.

### 2.2. *Depth reconstruction from $V_r$*

After stage-1, the multiple scattering forms dynamic speckle illumination following the Gaussian statistics.[19] The corresponding spatial frequency in speckle is band-limited in a Gaussian shape.

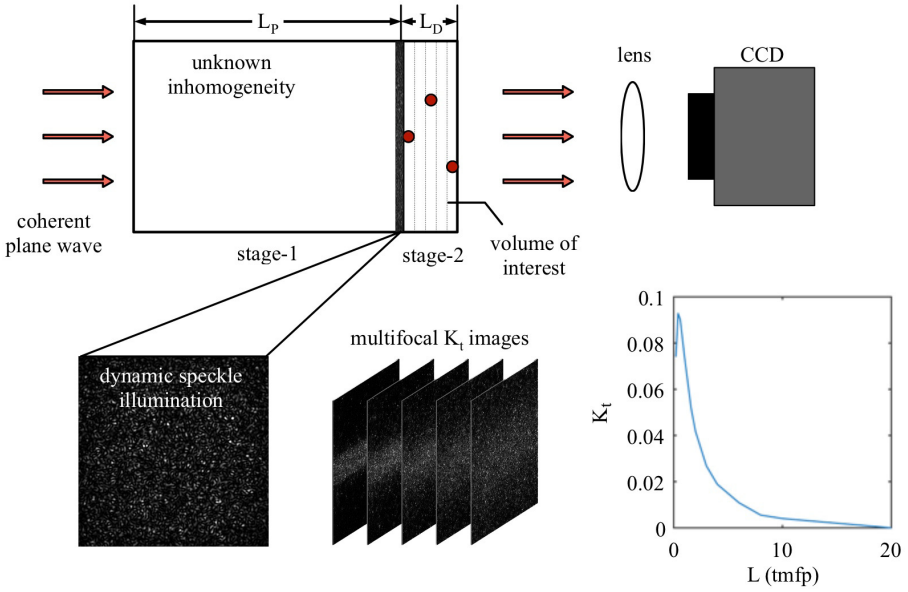


Fig. 1. Working principle of transmissive multifocal LSCI through thick tissue.

In stage-2, the speckle pattern is determined by both speckle illumination and tissue scattering. The flowing motion inside the vessel blurs the speckle pattern, i.e., widening the spatial frequency range due to spatial averaging. Meanwhile, the speckle in the surrounding tissue persists. Therefore, the change in speckle spatial frequency across the vessel boundary can be used for in-focus determination in coherent domain imaging. In practice, it is difficult to measure the modulation transfer function (MTF) and precisely quantify the spatial frequency. For the classical interference phenomenon, the visibility of interference fringes, i.e., $V = (I_{\max} - I_{\min})/(I_{\max} + I_{\min})$, is used as a characteristic parameter. For dynamic speckles, based on Gaussian statistics, we proposed a robust visibility parameter $V_r$ (Eq. (1)) as the estimation of the average spatial frequency changes across the vessel:

$$V_r = \frac{\langle I_{\max}\rangle_t - \langle I_{\min}\rangle_t}{\langle I\rangle_{st}}, \tag{1}$$

where the numerator $I_{\max} - I_{\min}$ is the range of the intensity in the spatial window across the boundary in a single speckle image $I_t(t)$. $\langle\cdot\rangle_t$ represents the temporal average, while $\langle\cdot\rangle_{st}$ represents the spatio-temporal average.

In stage-2, we use the electric-field MCS program to generate speckle images with vessels at different depths. The generated monochromatic speckle pattern then illuminates the phantom with overall $L_D = 2.5l_t$. The simulated tube (caliber 0.28 $l_t$) is positioned from the output surface down to 1.27 $l_t$ in depth. MFD is simulated by applying PSF with a 2D normal distribution. The PSF full width at half maximum (FWHM) increases with the out-of-focus depth when the focal plane is scanned along the $z$-direction. Figure 2(a) shows the calculated $V_r(z, z_0)$ topographies obtained from MCS. Each column in Fig. 2(a) shows the $V_r$ parameter at the same area (tube located at $z_0$) but different focal plane depths $z$. It is clear that $V_r$ of the same tube area reaches the minimum when the focal plane is at the actual depth.

To facilitate the depth estimation, we calculate the $1/V_r(z)^2$ instead in the vessel area (located at depth $z_0$) from MFD (focal plane at depth $z$). Figure 2(b) shows the $1/V_r(z)^2$ for the tube at three different depths by scanning the focal plane depth $z$. The Gaussian fitting reveals that $1/V_r(z)^2$ always reaches the maximum at $z = z_0$ and degrades with the out-of-focus distance $z - z_0$. Figure 2(c) shows that the focal position with maximum $1/V_r(z)^2$ provides a linear and robust estimation for the actual depth.

### 2.3. *Flow velocity mapping based on speckle contrast and depth*

For the tube area in the captured speckle images, $1/V_r(z)^2$ is calculated and thus used to estimate the tube depth. After obtaining the depth information, the in-focus speckle contrast images of vessels are used to estimate the relative flow velocity $v$.

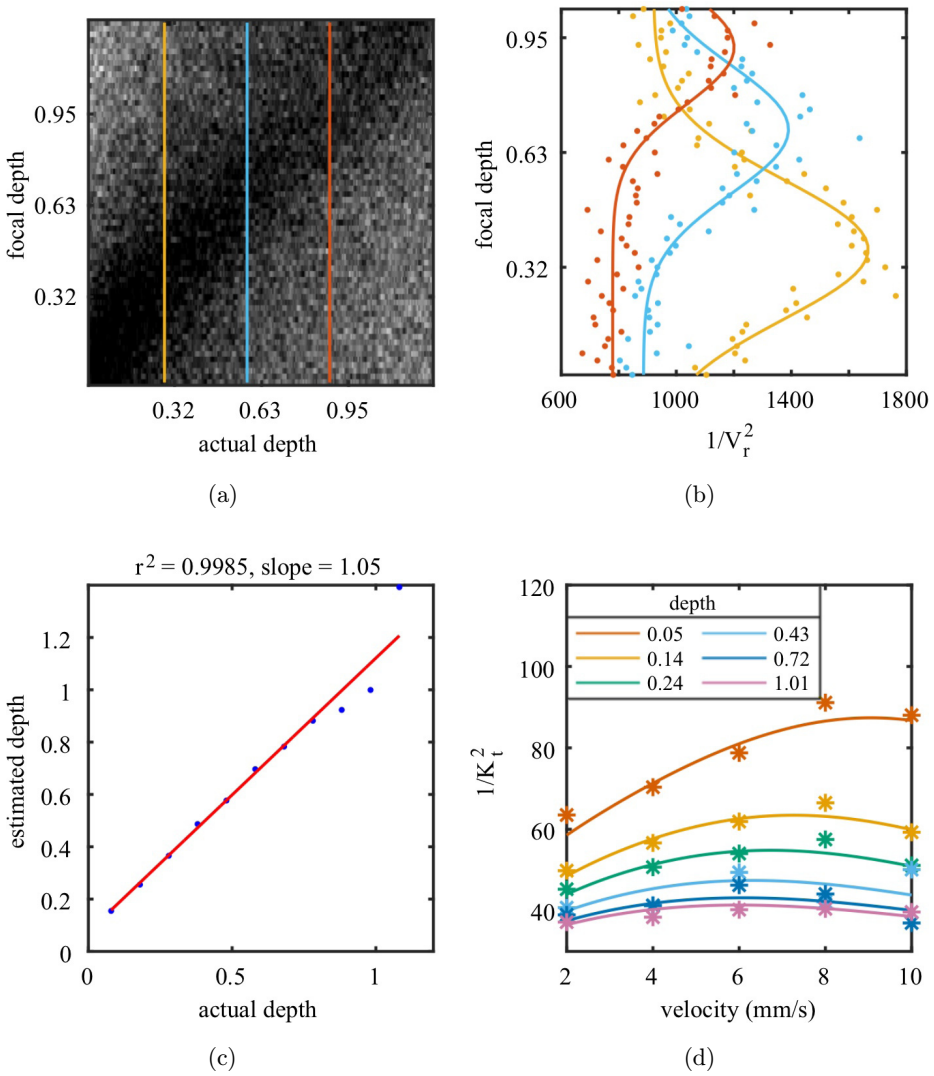


Fig. 2. (a) $V_r(z, z_0)$ topography calculated from MCS with an inclined tube phantom. Each column represents the $V_r$ parameter at the same tube area but by applying different focal plane depths $z$. (b) $1/V_r(z)^2$ along with focal depth ($z$) at 3 tube depths (i.e., $z_0 = 0.32l_t$ (yellow), $0.63l_t$ (blue), and $0.95l_t$ (red)). (c) Linear regression between the estimated depth (focal position with maximum $1/V_r(z)^2$) and actual depth ($z_0$). (d) Fitted $1/K_t^2$ for different velocities along the inclined tube phantom using the nonlinear least squares method ($R^2 = 0.91$). The depths ($0.05l_t$ to $1.01l_t$) are color coded.

The speckle contrast can be related to the intensity autocorrelation function $g_2(\tau)$ as follows:

$$K = \frac{\sigma_s}{\langle I \rangle} = \frac{2}{T}\int_0^T \left(1 - \frac{\tau}{T}\right)[g_2(\tau) - 1]d\tau, \qquad (2)$$

where $T$ is the exposure time, $\tau$ is the time lag. Under the ergodic assumption, the Siegert relation can be applied:

$$g_2(\tau) = 1 + \beta|g_1(\tau)|^2, \qquad (3)$$

where $\beta$ accounts for the global correlation loss due to speckle averaging and nonideality of the light source. The form of the field correlation function $g_1(\tau)$ for single scattering of Brownian motion or multiple scattering of ordered motion is given by

$$g_1(\tau) = \exp(-\tau/\tau_c). \qquad (4)$$

From Eqs. (2)–(4), the spatial speckle contrast can be related to the decorrelation time $\tau_c$ with the following equation:

$$K = \beta^{\frac{1}{2}}\left\{\frac{\tau_c^2}{2T^2}\left[e^{-\frac{2T}{\tau_c}} - 1 + \frac{2T}{\tau_c}\right]\right\}^{\frac{1}{2}}. \qquad (5)$$

When static scattering can't be negligible, the intensity autocorrelation function should include

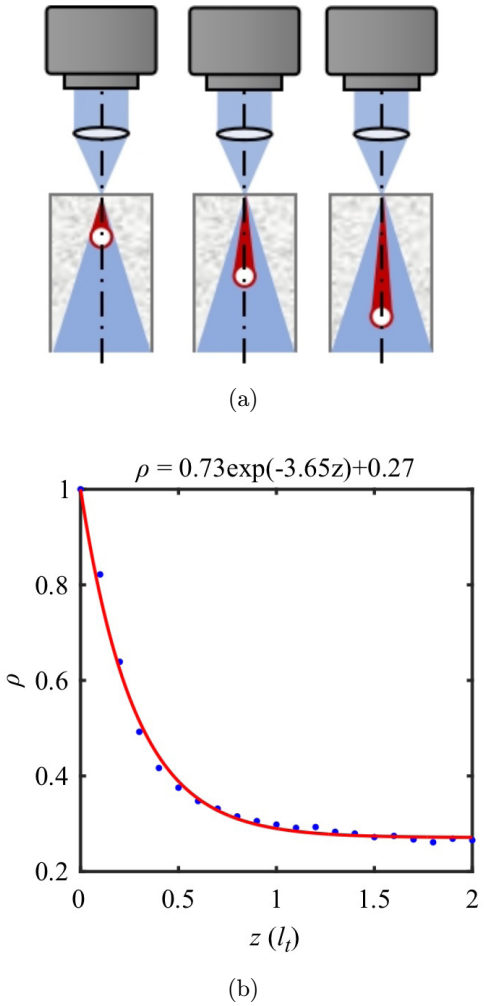


Fig. 3. (a) Monte Carlo configuration with cylinder dynamic sources at different depths. (b) Exponential relationship between dynamic fraction $\rho$ and depth $z$.

the dynamic scattering fraction $\rho$:

$$g_2(\tau) = 1 + \beta[\rho|g_1(\tau)| + (1-\rho)]^2, \tag{6}$$

where $\rho = \langle I_s(t)\rangle_t / (\langle I_s(t)\rangle_t + I_d)$. For transmissive imaging, $I_s(t)$ is the dynamically scattered light, presented as fluctuating speckle signals, while $I_d$ is the statically scattered light, which is recorded as the time-invariant diffusive background. We use MCS to evaluate the relation between the depth $z$ of a cylinder dynamic source and the detected dynamic fraction $\rho$, and fit with an exponential relationship between $\rho$ and $z$ (Fig. 3(b)):

$$\rho(z) = a\exp(-bz) + (1-a). \tag{7}$$

With a simplification of $x = T/\tau_c$, Eq. (5) can be further presented as depth-dependent speckle contrast-inverse decorrelation time model:

$$K(x,z) = \beta^{\frac{1}{2}}\Big\{\rho^2(z)\frac{e^{-2x}-1+2x}{2x^2} + 4\rho(z)(1-\rho(z))\frac{e^{-x}-1+x}{x^2} + (1-\rho(z))^2\Big\}^{\frac{1}{2}}. \tag{8}$$

## 3. Experiments

### 3.1. *In vitro phantom experiment*

The phantom medium (0.47% solidified Intralipid gel) was prepared with scattering properties $\mu_s' = 0.48\,\mathrm{mm}^{-1}$ (i.e., $l_t = 2.1\,\mathrm{mm}$). Intralipid emulsion with the same $\mu_s'$ was injected through the embedded PE tube (PE-50, outer diameter: 0.97 mm; inner diameter: 0.58 mm) at a depth of 0–4.76 $l_t$. The original focal plane was set to the top surface of the phantom. By moving the phantom up to 5 mm in a step of 0.5 mm, we are able to tune the focal plane down to a depth of 2.38 $l_t$ within the phantom. The flow velocity within the PE tube was controlled at 0–10 mm/s with a programmable syringe pump.

### 3.2. *In vivo experiment*

Fertilized chicken eggs were obtained from a local farmers' market and incubated at 60% humidity and 37.8°C at a rotation rate of 360°/2 h. On embryonic Day 3, we punctured a small hole on the wide end of the egg, where the air sac was located, using the tip of pointed scissors. A round window was then prepared for imaging by carefully removing shell fragments and membranes around the hole. Another small hole for inserting the fiber was made approximately 2 mm below the window with an intact membrane. The fiber was fixed by dental cement and connected to a 785 nm fiber laser. The egg was placed on a sample holder for imaging.

The transmissive multifocal LSCI setup is shown in Fig. 4(a). A 785 nm diode laser (model: S1FC785, Thorlabs) was coupled into the single-mode fiber to illuminate the volume of interest. Speckle patterns were formed by random interference of scattered light through the sample and collected by the imaging lens coupled to the CCD camera (model: scA640-70fm, Basler). Multifocal imaging was achieved by adjusting the relative axial position of

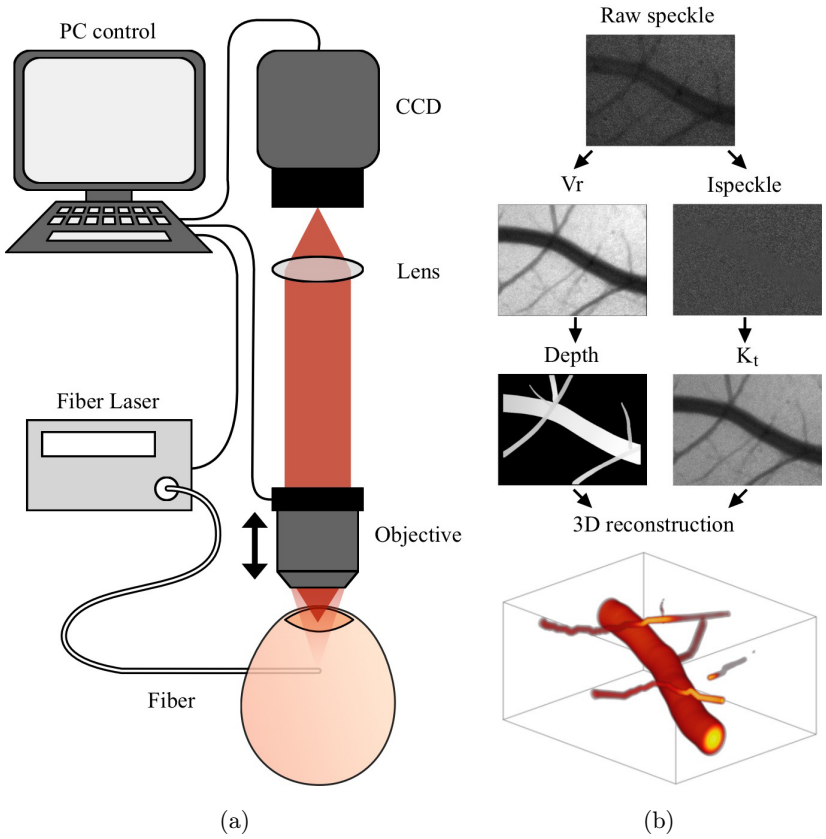


Fig. 4. (a) Schematic of *in vivo* imaging experiment. (b) Data processing pipelines.

the sample from the lens. Multifocal images were taken at a focal step of 200 $\mu$m below the surface for a depth range of 2 mm at a magnification of 3×. On each focal plane, a sequence of 100 raw speckle images were recorded under a 5 ms exposure time and 50 fps frame rate.

## 4. Results

We first validate the depth estimation strategy and the depth-dependent contrast to velocity model by an *in vitro* phantom experiment. The relationship between $1/K^2$ and the actual velocities is shown in Fig. 2(d). The data are fitted to Eq. (8) very well using the nonlinear least-squares method (adjusted $R^2 = 0.91$). The superficial structures demonstrate a larger dynamic range with better linearity between $1/K^2$ and velocity $v$. In transmissive imaging, the relation between $1/K^2$ and velocity $v$ demonstrates a "banana shape" (Fig. 2(d)). The decrease tendency at higher velocity results in underestimated flow when using the conventional contrast model. Our new model, however, fits well with the $1/K^2$ at different depths and velocities by compensating for the lower dynamic fraction in deeper structure.

Next, we further test the method in an *in vivo* chicken embryo experiment as one of the possible application scenarios for transmissive imaging. Chicken embryos have been widely used as a model in cardiac development for their convenience in investigating hemodynamics and angiogenesis. On each focal plane, raw speckle images are first used to calculate $V_r(z)$. Masks for different vessels are manually segmented across all focal planes. Vessel centerlines are extracted, and the Euclidean distance transform of the inverse mask is calculated to identify the vessel radius. The $1/V_r(z)^2$ parameters of each centerline point in different focal planes are compared, and the maximum value indicates the vessel depth. Speckle images are then processed by temporal laser speckle contrast analysis to obtain $K_t$. The relative blood flow (rBF) is then calculated as $v \propto x = T/\tau_c$ based on the model $K_t(v, z_d)$ in Eq. (8). By assuming a laminar and parabolic flow profile crossing the vessel, we are able to resolve the velocity profile and remap it to the 3D vascular structures.

The reconstructed 3D vessel structure and flow distribution are shown in Fig. 5(a) (also see the supplementary video). The vessel branches, e.g., $v1$ from $v2$, $v4$ from $v3$, are clearly identified. The spatial relation between $v1$ and $v6$ can also be demonstrated when the traditional LSCI fails. Figure 5(b) shows the maximum projection image of reconstructed blood flow, which significantly

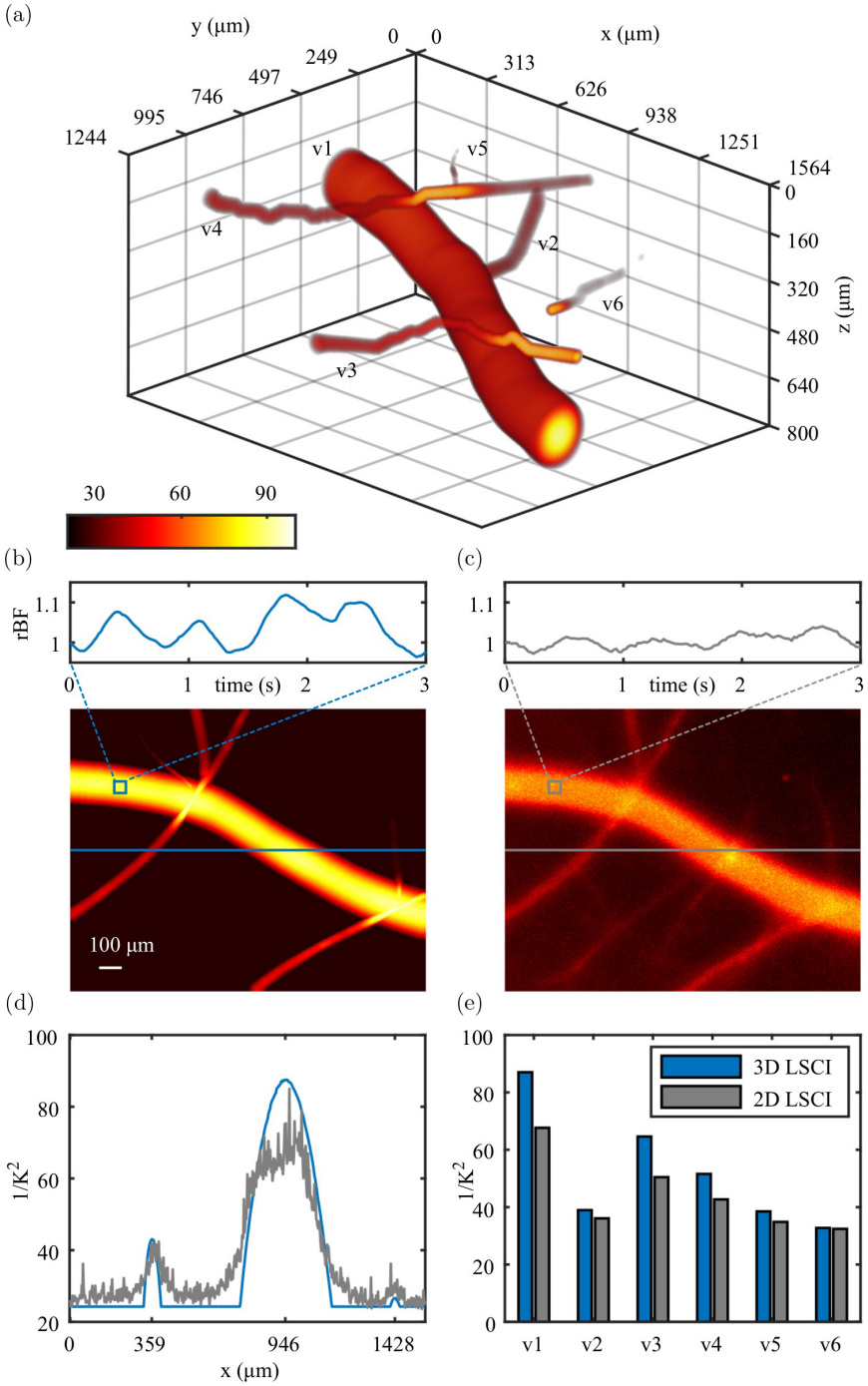


Fig. 5. 3D reconstruction of vasculature and blood flow in a chick embryo (a). Based on the reconstructed 3D blood flow and the raw multifocal $1/K^2$ images, the maximum projection images of a 1.56 mm × 1.24 mm field of view and the mean relative blood flow fluctuations within a 50 $\mu$m × 50 $\mu$m ROI are shown in (b) and (c), respectively, exhibiting a heartbeat signal at approximately 80 bpm. Flow profiles along a horizontal line in (b) and (c) are compared in (d). The rBF indices in six vessel segments (v1–v6) are also shown in (e).

improves the imaging SNR compared to that of raw multifocal $1/K_t^2$ stacks (Fig. 5(c)). The heart-beating-induced[20] mean rBF changes in the 3D reconstruction (Fig. 5(b)) were clearly retrieved in comparison to that by traditional 2D LSCI method (Fig. 5(c)). The blood flow profiles are well-described by our reconstruction shown in Fig. 5(d). Furthermore, we evaluated the rBF index in six selected vessel segments (Fig. 5(e)), showing consistent underestimation by the traditional 2D LSCI method (gray) compared with our 3D reconstruction (blue), especially in deeper structures ($v1$, $v6$).

## 5. Discussion

In this study, we reconstructed 3D vasculature and blood flow in thick embryonic tissue using transmissive multifocal LSCI. The proposed strategy can be applied to mice or even human tissue for *in vivo* imaging. However, laser delivery needs accordingly be optimized to satisfy the safety in clinical applications. The effective depth of 3D imaging $L_D$ is limited by the optical properties of the tissue, (i.e., $\mu_a$ and $\mu_s'$), determined by both tissue properties and illumination wavelength. Usually, longer wavelengths in the near-infrared range (i.e., NIR-I or NIR-II) have larger $l_t$ and can obtain deeper reconstruction. The detection SNR is one of the factors in extending the overall thickness $L$; thus, scientific cameras, e.g., sCMOS cameras or single photon counting camera,[21] can be utilized. The transmissive multifocal LSCI method utilizes $1/V_r(z)^2$ as the depth estimator derived from the interference nature of speckle. A more robust parameter or strategy should be developed to increase the precision of depth estimation for coherent domain imaging. The temporal coherence of the light source is also critical for resolving the depth information. Wider line-width or instability in laser source would fail to detect the speckle pattern after more than 10 $l_t$ propagation.

Our method retrieves blood flow information in 3D volumes, compensating for the underestimation in deeper structures. However, in transmissive optical imaging, it is difficult to distinguish dynamic scattering with mixed depths at the same lateral location; that is, if there are overlapping vascular structures, the reconstructed local blood flow will be overestimated in both vessels. Introducing multiple illumination detection angles may help to separate dynamic information from different sources. For imaging thick biological tissue, the relationship between DFD features and object depth $z$ is also affected by intensity attenuation due to absorption, which needs further correction.[22]

Compared to other 3D blood flow imaging methods, such as optical coherence tomography angiography[23] and speckle contrast optical tomography,[24] our method preserves wide-field imaging and saves line scan time. The focal scanning time can be further saved by applying a multifocal adapter[8,9] to image all focal planes in a single shot, which should improve the time resolution of this method to a level of traditional speckle imaging. Applying the state-of-art auto-segmentation method,[25] real-time 3D imaging can be realized with a relatively simple configuration.

## 6. Conclusions

In conclusion, we proposed a transmissive multifocal LSCI method for thick tissue ($> 4l_t$). Both depth information and corrected blood flow are obtained within the $2l_t$ depth beneath the imaging surface. The theoretical framework is validated by both MCS and *in vitro* phantom experiments. *In vivo* imaging of chick embryos was also demonstrated, showing their potential in other biomedical applications.

## Acknowledgments

The study was supported by National Natural Science Foundation of China (NSFC No. 61876108) and the National Key Research & Development Program of Ministry of Science and Technology of the People's Republic of China (Grant Nos. 2018YFC2002300, 2018YFC2002303).

## Conflict of Interest

The authors declare no conflicts of interest relevant to this article.

## References

1. D. A. Boas, A. K. Dunn, "Laser speckle contrast imaging in biomedical optics," *J. Biomed. Opt.* **15**(1), 011109 (2010).
2. P. Miao, N. Li, N. V. Thakor, S. Tong, "Random process estimator for laser speckle imaging of

cerebral blood flow," *Opt. Express* **18**(1), 218–236 (2010).
3. W. Heeman, W. Steenbergen, G. M. van Dam, E. C. Boerma, "Clinical applications of laser speckle contrast imaging: A review," *J. Biomed. Opt.* **24**(8), 080901 (2019).
4. S. M. S. Kazmi, E. Faraji, M. A. Davis, Y.-Y. Huang, X. J. Zhang, A. K. Dunn, "Flux or speed? Examining speckle contrast imaging of vascular flows," *Biomed. Opt. Express* **6**(7), 2588–2608 (2015).
5. M. A. Davis, S. M. S. Kazmi, A. K. Dunn, "Imaging depth and multiple scattering in laser speckle contrast imaging," *J. Biomed. Opt.* **19**(8), 1–10 (2014).
6. P. Miao, Z. Chao, Y. Zhang, N. Li, N. V. Thakor, "Entropy analysis reveals a simple linear relation between laser speckle and blood flow," *Opt. Lett.* **39**(13), 3907–3910 (2014).
7. D.-Y. Li, Q. Xia, T.-T. Yu, J.-T. Zhu, D. Zhu, "Transmissive-detected laser speckle contrast imaging for blood flow monitoring in thick tissue: from monte carlo simulation to experimental demonstration," *Light Sci. Appl.* **10**(1), 1–15 (2021).
8. J. N. Hansen, A. Gong, D. Wachten, R. Pascal, A. Turpin, J. F. Jikeli, U. B. Kaupp, L. Alvarez, "Multifocal imaging for precise, label-free tracking of fast biological processes in 3D," *Nat. Commun.* **12**(1), 4574 (2021).
9. S. Zheng, S. Xiao, L. Kretsge, A. Cruz-Martín, J. Mertz, "Depth resolution in multifocus laser speckle contrast imaging," *Opt. Lett.* **46**(19), 5059–5062 (2021).
10. I. Sigal, R. Gad, A. M. Caravaca-Aguirre, Y. Atchia, D. B. Conkey, R. Piestun, O. Levi, "Laser speckle contrast imaging with extended depth of field for *in-vivo* tissue imaging," *Biomed. Opt. Express* **5**(1), 123–135 (2014).
11. D. Ringuette, I. Sigal, R. Gad, O. Levi, "Reducing misfocus-related motion artefacts in laser speckle contrast imaging," *Biomed. Opt. Express* **6**(1), 266–276 (2015).
12. E. Du, S. Shen, A. Qiu, N. Chen, "Depth-dependent microscopic flow imaging with line scan laser speckle acquisition and analysis," in *Optics in Health Care and Biomedical Optics XI*, Q. Luo, X. Li, Y. Gu, D. Zhu, Eds., pp. 20–26, International Society for Optics and Photonics (2021).
13. C. Liu, K. Kiliç, S. E. Erdener, D. A. Boas, D. D. Postnov, "Choosing a model for laser speckle contrast imaging," *Biomed. Opt. Express* **12**(6), 3571–3583 (2021).
14. A. B. Parthasarathy, W. J. Tom, A. Gopal, X. Zhang, A. K. Dunn, "Robust flow measurement with multi-exposure speckle imaging," *Opt. Express* **16**(3), 1975–1989 (2008).
15. Y. Zhang, C. Wang, S. Tong, P. Miao, "Separating single-and multiple-scattering components in laser speckle contrast imaging of tissue blood flow," *Biomed. Opt. Express* **13**(5), 2881–2895 (2022).
16. D. D. Postnov, J. Tang, S. E. Erdener, K. Kılıç, D. A. Boas, "Dynamic light scattering imaging," *Sci. Adv.* **6**(45), eabc4628 (2020).
17. C. Z. Jafari, C. T. Sullender, D. R. Miller, S. A. Mihelic, A. K. Dunn, "Effect of vascular structure on laser speckle contrast imaging," *Biomed. Opt. Express* **11**(10), 5826–5841 (2020).
18. D. D. Postnov, X. Cheng, S. E. Erdener, D. A. Boas, "Choosing a laser for laser speckle contrast imaging," *Sci. Rep.* **9**(1), 1–6 (2019).
19. P. Miao, Y. Zhang, C. Wang, S. Tong, "Random matrix description of dynamically backscattered coherent waves propagating in a wide-field-illuminated random medium," *Appl. Phys. Lett.* **120**(4), 043701 (2022).
20. H. Tazawa, S. Nakagawa, "Response of egg temperature, heart rate and blood pressure in the chick embryo to hypothermal stress," *J. Comp. Physiol. B* **155**(2), 195–200 (1985).
21. T. Dragojević, D. Bronzi, H. M. Varma, C. P. Valdes, C. Castellvi, F. Villa, A. Tosi, C. Justicia, F. Zappa, T. Durduran, "High-speed multi-exposure laser speckle contrast imaging with a single-photon counting camera," *Biomed. Opt. Express* **6**(8), 2865–2876 (2015).
22. K. Khaksari, S. J. Kirkpatrick, "Combined effects of scattering and absorption on laser speckle contrast imaging," *J. Biomed. Opt.* **21**(7), 076002 (2016).
23. R. F. Spaide, J. G. Fujimoto, N. K. Waheed, S. R. Sadda, G. Staurenghi, "Optical coherence tomography angiography," *Prog. Retin. Eye Res.* **64**, 1–55 (2018).
24. H. M. Varma, C. P. Valdes, A. K. Kristoffersen, J. P. Culver, T. Durduran, "Speckle contrast optical tomography: a new method for deep tissue three-dimensional tomography of blood flow," *Biomed. Opt. Express* **5**(4), 1275–1289 (2014).
25. H. Chen, Y. Shi, B. Bo, D. Zhao, P. Miao, S. Tong, C. Wang, "Real-time cerebral vessel segmentation in laser speckle contrast image based on unsupervised domain adaptation," *Front. Neurosci.* **15**, 755198 (2021).